AGU PUBLICATIONS

JGR

Journal of Geophysical Research: Atmospheres

RESEARCH ARTICLE
10.1002/2015JD024643

Key Points:
- RHI in cirrus clouds varies seasonally, with the overall highest RHI observed in the winter
- RHI values frequently exceed 100% in cirrus clouds for all atmospheric states
- The overall occurrence of cirrus clouds is more closely tied to dynamical regimes than RHI

Correspondence to:
A. M. Dzambo,
dzamboam@gmail.com

Citation:
Dzambo, A. M., and D. D. Turner (2016), Characterizing relative humidity with respect to ice in midlatitude cirrus clouds as a function of atmospheric state, *J. Geophys. Res. Atmos.*, *121*, 12,253–12,269, doi:10.1002/2015JD024643.

Received 11 DEC 2015
Accepted 15 SEP 2016
Accepted article online 17 SEP 2016
Published online 24 OCT 2016

Characterizing relative humidity with respect to ice in midlatitude cirrus clouds as a function of atmospheric state

Andrew M. Dzambo[1] and David D. Turner[2]

[1]Cooperative Institute for Mesoscale Meteorological Studies, University of Oklahoma, Norman, Oklahoma, USA, [2]National Severe Storms Laboratory/NOAA, Norman, Oklahoma, USA

Abstract Midlatitude cirrus cloud macrophysical and microphysical properties have been shown in previous studies to vary seasonally and in various large-scale dynamical regimes, but relative humidity with respect to ice (RHI) within cirrus clouds has not been studied extensively in this context. Using a combination of radiosonde and millimeter-wavelength cloud radar data, we identify 1076 cirrus clouds spanning a 7 year period from 2004 to 2011. These data are separated into five classes using a previously published algorithm that is based largely on synoptic conditions. Using these data and classification scheme, we find that RHI in cirrus clouds varies seasonally. Variations in cirrus cloud RHI exist within the prescribed classifications; however, most of the variations are within the measurement uncertainty. Additionally, with the exception of nonsummer class cirrus, these variations are not statistically significant. We also find that cirrus cloud occurrence is not necessarily correlated with higher observed values of RHI. The structure of RHI in cirrus clouds varies more in thicker clouds, which follows previous studies showing that macrophysical and microphysical variability increases in thicker cirrus clouds.

1. Introduction

Cirrus clouds cover approximately 30% of the globe [*Liou*, 1986] and hence represent a critical part of the global climate system [*Stephens et al*., 2002]. Their spatial extent varies with climate; for example, cirrus clouds are observed in tropical locations around ~44% of the time compared to ~24% of the time in midlatitude locations [*Kalesse and Kollias*, 2013]. Cirrus clouds have known impacts on the Earth's radiative budget [*Ackerman et al*., 1988; *Yang et al*., 2001; *Baran et al*., 2014], water vapor transport in the upper troposphere/lower stratosphere [*Pfister et al*., 2001], stratospheric dehydration [*Potter and Holton*, 1995], and even atmospheric chemistry processes [*Bogdan and Molina*, 2009]. The particle shape, concentration, vertical distribution, and particle size distribution of ice crystals in cirrus clouds directly affect the magnitude of these impacts. Precise knowledge of these processes and variables is required for accurate parameterization in global climate models [e.g., *Mitchell et al*., 2011] and numerical weather prediction models [e.g., *Furtado et al*., 2014].

Observational and modeling studies of cloud macrophysical/microphysical properties are critical to reducing the uncertainty in climate model output, especially since idealized radiative transfer approximations and cloud macrophysical/microphysical quantities are used as input [*Sassen and Campbell*, 2001]. These approximations and quantities are inherently derived from observational studies; however, when using characteristic approximations and quantities, the user must consider if replicating observational studies (for example) for different locations would yield different results (potentially changing the said approximations and quantities). For example, in *Sassen and Campbell* [2001], cirrus clouds observed from a 10 year data set from the University of Utah's Facility for Atmospheric Remote Sensing (Salt Lake City, Utah, USA) had an average thickness of 1.81 km, cloud base and top temperatures of −34.4°C and −53.9°C (respectively), and cloud base and top heights at 8.8 and 11.2 km (respectively). By comparison, *Mace et al*. [2001] used a 1 year data set of millimeter-wavelength cloud radar (MMCR) measurements [*Moran et al*., 1998] and found that cirrus clouds over the Atmospheric Radiation Program's (ARM) Southern Great Plains (SGP) site (Lamont, OK, USA) had an average thickness of 2.0 km and generally occurred between 8.5 and 10 km above ground level. The generation and maintenance of midlatitude cirrus clouds, using the two aforementioned studies as an example, are strongly dependent on regional characteristics (e.g., topography) and weather patterns [*Sassen and Campbell*, 2001].

Physical parameterizations for a grid box in a climate model assume some a priori knowledge of the physical processes in the grid box, especially since cirrus cloud properties (often represented by probability density functions) are correlated to dynamical regimes [*Mace et al*., 2006]. Dynamical regimes over the U.S. Southern Great Plains vary seasonally, and given that climate models do not explicitly predict weather events as would be expected for a given location, attempting to parse differences between climate model outputs for cloud and precipitation processes and dynamical regimes is particularly challenging [*Marchand et al*., 2009]. As a result, several studies have attempted to characterize cloud properties (e.g., thickness and hydrometeor occurrence and type) as a function of climatology [e.g., *Mace et al*., 2001, 2006] and atmospheric state [e.g., *Mace et al*., 1995; *Sassen and Campbell*, 2001; *Marchand et al*., 2009; *Berry and Mace*, 2013]. It should be noted that the aforementioned and related studies cover various regions across the globe and not just for the U.S. midlatitude locations. In the U.S. Southern Great Plains, dynamical and thermodynamical regimes vary dramatically throughout the year compared to, for example, a tropical location. This is reflected in studies that characterize the large-scale atmospheric state for these climatologically distinct locations: using long-term data sets, 21 distinct atmospheric states were determined for the ARM SGP site [*Marchand et al*., 2009; *Evans and Marchand*, 2013] versus 8 distinct states for a tropical location [*Evans et al*., 2012]. Disseminating differences between environmental properties conducive for cloud formation (such as large-scale ascent) therefore is considerably more complicated at midlatitude locations such as the ARM SGP site.

One requisite environmental condition needed for new ice crystal nucleation and subsequent growth is saturation of relative humidity with respect to ice (RHI hereafter) [*Heymsfield and Miloshevich*, 1995]. In the upper troposphere, RHI saturation can be achieved through a number of processes such as uplifting moisture over an upper level ridge [*Evans and Marchand*, 2013], rapid wave-like fluctuations of temperature analogous to gravity wave activity [*Haag et al*., 2003], and adiabatic cooling by large-scale uplift in the outflow region of a warm conveyor belt [*Spichtinger et al*., 2005]. These processes have been linked to increased cirrus cloud occurrence in several studies [e.g., *Sassen and Campbell*, 2001; *Mace et al*., 2006] though these processes do not always explain microphysical variability within cirrus [*Muhlbauer et al*., 2014]. Rather, variability in RHI could be a primary driver of microphysical variability although more investigation is needed to prove this [*Muhlbauer et al*., 2014].

While the importance of RHI to cirrus cloud occurrence and maintenance are well understood qualitatively, quantifying RHI presents numerous challenges. Observational studies involving RH/RHI are particularly difficult because of large uncertainties in the measurements themselves. Radiosonde measurements of RH have the best vertical resolution (~10 m) but suffer from large measurement uncertainty of 5% and, in the case of daytime measurements for some sensors, have a well-documented dry bias induced by solar radiation [e.g., *Vömel et al*., 2007; *Miloshevich et al*., 2009; *Wang et al*., 2013]. Raman lidar measurements of water vapor, unlike radiosondes, are not subject to dry-biased measurements but result in RH uncertainties of approximately 10% [*Turner et al*., 2007]. By comparison, model-reanalysis data sets such as European Center for Medium-Range Weather Forecasting (ECMWF) ERA-Interim reanalysis are readily available and offer complete analyses (e.g., wind, temperature, and RH for specified height/pressure resolution) but rely on interpolation to resolve quantities between model grid cells. *Ovarlez et al*. [2000] showed that ECMWF model-reanalysis data underestimated RHI for low-temperature, humid conditions but captured the structure of RHI (and water vapor mixing ratio) fairly well. Many studies have used RH/RHI data from sources such as model-derived RH/RHI data [e.g., *Berry and Mace*, 2013], aircraft measurements [e.g., *Heymsfield and Miloshevich*, 1995], and Raman lidar [e.g., *Comstock et al*., 2004] to aid in their analysis of cirrus cloud properties and processes. To our knowledge, however, a long-term observational study of RHI measurements in midlatitude cirrus clouds, especially when accounting for differing thermodynamic and dynamical regimes, has not been done and thus is a key part of our study.

The goal of our study is to characterize RHI in cirrus clouds as a function of season and atmospheric state using observational data sets and to assess any differences in RHI among the specified atmospheric states. This study takes advantage of long-term ARM observational data sets from the MMCR and radiosonde, where the moisture measurements from the latter were corrected using a recently published solar radiative dry bias correction algorithm. Using these data sets allows any implications from the results (such as statistically higher/lower RHI among distinct atmospheric states) to be well characterized in terms of measurement accuracy and uncertainty. Ultimately, our study addresses the following questions:

1. Given measurements of in-cloud, clear-sky, and above-cloud RHI over a sufficient period of time, do seasonal variations in RHI exist?
2. How does RHI vary as a function of atmospheric state? If RHI varies significantly among atmospheric states, can it be explained by seasonal differences?
3. If variations in RHI exist, whether by season or between atmospheric states, how do these variations compare to the uncertainty of the RHI measurements?

The next section describes details regarding our definition of a cirrus cloud, our database of cirrus clouds (derived from MMCR measurements), collocation of radiosonde and MMCR measurements, and the atmospheric state classification algorithm used to segregate dynamical and thermodynamical regimes.

2. Data and Methods

This study used data from 7 years of observations collected at the Atmospheric Radiation Measurements (ARM) program's Southern Great Plains (SGP) site [*Ackerman and Stokes*, 2003; *Sisterson et al*., 2016] located near Lamont, OK (36°, 36′, 18″N; 97°, 29′, 6.0″W). Data from this site are ideal for the study of midlatitude cirrus clouds because of its location near the geographical center of the United States and the wide variety of weather conditions experienced year round. This study makes heavy use of MMCR data [*Moran et al*., 1998; *Clothiaux et al*., 1999; *Kollias et al*., 2007], Vaisala RS92 radiosonde data [*Währn et al*., 2004; *Wang et al*., 2013], and an atmospheric state classification algorithm [*Marchand et al*., 2009; *Evans and Marchand*, 2013]. The following sections describe these data sets in more detail.

2.1. Millimeter-Wavelength Cloud Radar

The MMCR is a zenith pointing radar designed to measure the vertical occurrence of clouds, characterize the microphysical composition of clouds, and to provide a detailed, long-term and continuous data set for nonprecipitating and weakly precipitating clouds [*Moran et al*., 1998]. This instrument operates at a frequency of 34.86 GHz (8.7 mm) and can measure radar reflectivity, Doppler velocity, and Doppler spectrum width [*Kollias et al*., 2005]. The MMCR has four operation modes, each of which has different strengths and weaknesses depending on the application [*Moran et al*., 1998], and these modes are interleaved at regular intervals. MMCR Mode 2 data are the "cirrus" mode: pulse compression encoding gives the MMCR extra sensitivity, allowing it to measure echoes as low as −50 dBZ. The dynamic range of the MMCR is from −50 dBZ to 20 dBZ and has a vertical resolution of 90 m. Updated operational modes with increased temporal resolution have been tested and developed for the MMCR [*Kollias et al*., 2007]; however, updated Mode 2 data were not available for use in this study. Regardless, the existing Mode 2 data remain a highly valuable tool for characterizing cirrus clouds and hence is the data set of choice.

2.2. Vaisala RS92 Radiosondes

Radiosondes are balloon-borne measurement devices that measure profiles of temperature, humidity, and wind and are known for their exceptionally high vertical resolution (~10 m). Vaisala RS92 radiosondes are among the most widely used radiosondes in the world and are used by around 30% of all global radiosonde stations [*Wang et al*., 2013]. The high vertical resolution of Vaisala RS92 radiosondes as well as the availability of this data (sondes of this type are launched four times per day at the ARM SGP site) makes this instrument particularly appealing for the study of cirrus clouds.

The RS92 measures temperature using a thin capacitive wire sensor, where the measured voltage of the sensor is proportional to the temperature. Temperature measurements are accurate to 0.2°C from the surface to 100 hPa, while above 100 hPa radiosonde temperature measurements are accurate to 0.3°C (http://www.vaisala.com/Vaisala%20Documents/Brochures%20and%20Datasheets/RS92SGP-Datasheet-B210358EN-F-LOW.pdf). The total uncertainty in the temperature measurements is 0.5°C. RH measurements are made using a pair of thin-film capacitive elements, where the measured capacitance of these elements is proportional to the number of water vapor molecules in contact with the sensor. Radiosonde RH data have a total uncertainty of 5% (additional uncertainty information can be found online in the website provided for the temperature data). Using radiosonde temperature and RH data and noting that over 97% of our data occurs in atmospheric layers warmer than −60C, saturation vapor pressure with respect to ice is computed using the Goff-Gratch equation [*Goff and Gratch*, 1946]:

$$\log_{10}(e_{si}) = 9.09718\times\left(\frac{273.15}{T}-1\right) - 3.56654\times\log_{10}\left(\frac{273.15}{T}\right) + 0.876793\times\left(1-\frac{T}{273.15}\right) + \log_{10}(6.1071) \quad (1)$$

After converting RH to vapor pressure (denoted e), RHI is computed with the following formula:

$$\mathrm{RHI} = \frac{e}{e_{si}}\times 100\% \quad (2)$$

Vaisala RS92 radiosonde RH data, especially before 2012, are known to be dry biased in the middle and upper troposphere [*Vömel et al*., 2007]. The primary source of the RH dry bias is from solar radiative heating of the humidity sensor [*Vömel et al*., 2007], while another (lesser) source of uncertainty includes errors in the calibration model [*Miloshevich et al*., 2009]. The temporal response time of the sensor, known as time lag, is another potential source of uncertainty but is not considered because it contributes, at most, 1–2% error in RH [*Wang et al*., 2013; *Dzambo et al*., 2016] and has a mean error of 0% [*Dzambo et al*., 2016]. A number of RS92 RH correction algorithms have been developed [e.g., *Cady-Pereira et al*., 2008; *Yoneyama et al*., 2008; *Rowe et al*., 2008; *Miloshevich et al*., 2009; *Wang et al*., 2013]. We advocate the use of the correction algorithms proposed by *Miloshevich et al*. [2009] and *Wang et al*. [2013], both of which are height-dependent corrections, for two reasons (results not shown) [*Dzambo et al*., 2016]:

1. Both algorithms significantly improve the radiosonde's RH profile such that precipitable water vapor (PWV) derived from the *Miloshevich et al*. [2009] and *Wang et al*. [2013]. (The improvement in PWV for the *Wang et al*. [2013] RH correction algorithm (using PWV derived from a two-channel microwave radiometer) was also shown in *Yu et al*. [2015].) RH-corrected profiles is in much better agreement with the PWV retrieved from ground-based microwave radiometers [*Turner et al*., 2007], whereas the PWV derived from the original (uncorrected) radiosonde shows a large dry bias.
2. Computed infrared radiances using the *Miloshevich et al*. [2009] and *Wang et al*. [2013] corrected profiles as input compare better to AIRS radiance observations in water vapor sensitive wave numbers (i.e., 1300 to 2000 cm^{-1}) than model-computed radiances derived from uncorrected RH measurements. The *Wang et al*. [2013] RH correction decreases the bias in model-computed brightness temperatures (compared to AIRS) between 0.2 and 0.3 K, while the *Miloshevich et al*. [2009] correction decreases this bias by 0.2 to 0.5 K.

Ultimately, we chose to use the *Wang et al*. [2013] RH correction algorithm in this work because the correction was developed using both clear- and cloudy-sky observations. The *Miloshevich et al*. [2009] algorithm is intended for mainly clear skies. The use of the *Wang et al*. [2013] algorithm makes practical sense considering that the focus is on cirrus clouds. The RH correction formula and all constants are defined in section 2b of *Wang et al*. [2013].

2.3. Cirrus Cloud Detection Algorithm

To get the best possible representation of cirrus clouds from the 7 years of data available to us, we designed an algorithm that captures cirrus cloud "events" from the MMCR data set. Although MMCR Mode 2 data are sensitive to echoes as low as −50 dBZ, we used −35 dBZ as a lower limit to minimize noisy measurements. Furthermore, we used the following criteria (with the reflectivity measurements) as a baseline for our definition of a cirrus cloud event:

1. The minimum altitude in which we define a cirrus cloud is dependent on the height of the troposphere:
   a. The height of the troposphere is determined from radiosonde measurements and interpolated to match the time resolution of the MMCR (i.e., ~10 s).
      i. The minimum altitude is determined between these two methods: (i) 55% of the height of the troposphere and (ii) the first altitude where the temperature decreases below −10°C.
      ii. If the minimum altitude was determined based on the fractional height of the troposphere, the height is recorded as a minimum threshold. If the temperature criteria were used, the maximum altitude is determined through the following two methods: (i) 50% of the height of the troposphere and (ii) the first altitude where the temperature decreases below −10°C.
2. There is no minimum thickness requirement, but reflectivity measurements must be (at minimum) contiguous at the altitude of the reflectivity measurement at ±90 m from the previous time step for a minimum of 15 min.

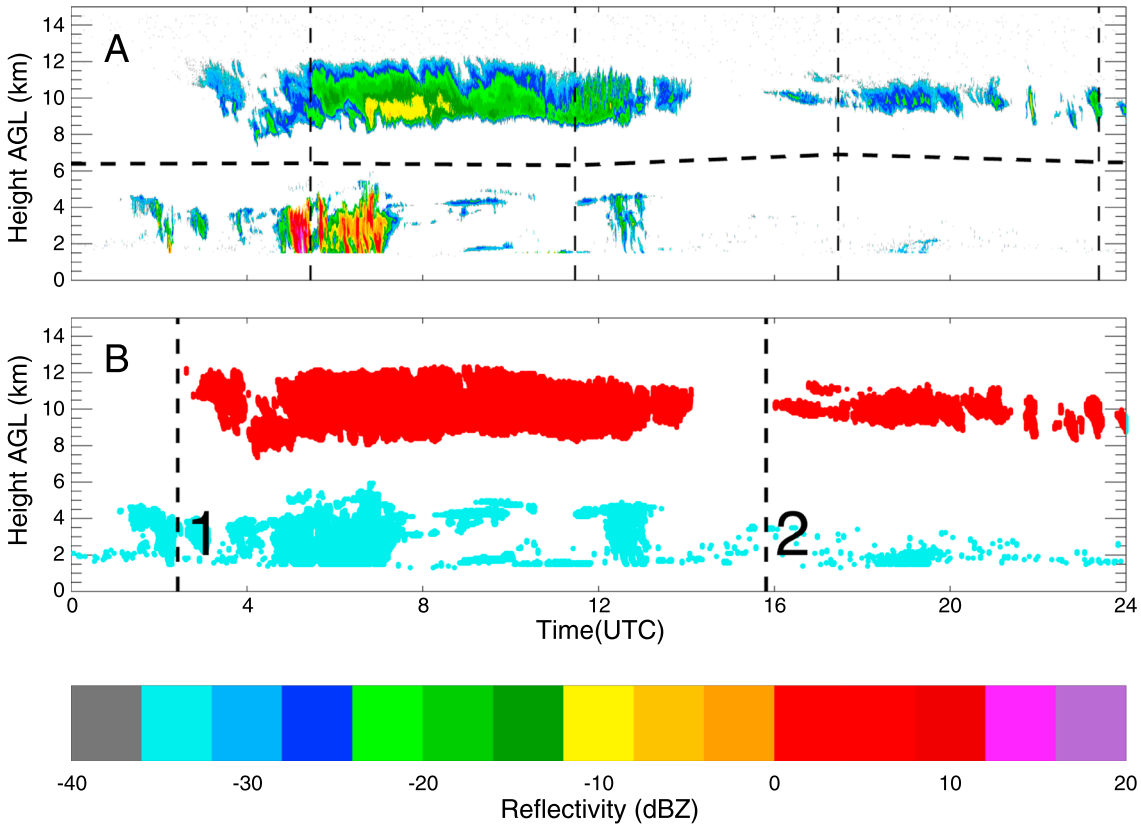

Figure 1. (a) MMCR reflectivity measurements and (b) cloud masks (cirrus cloud masks are colored red) for 3 June 2009 at the ARM SGP site. The dashed line in Figure 1a represents the minimum height threshold (the method is described in the text). The vertical dashed lines in Figure 1a represent the 05Z, 11Z, 17Z, and 23Z radiosonde launch times (respectively) after accounting for time lag, as described in the text. The vertical dashed lines in Figure 1b represent the beginning of two cirrus cloud events.

3. An event ends under one of the following two subcriteria:
   a. When no contiguous reflectivity measurements are found within 30 min of the last set of reflectivity measurements (i.e., gaps of less than 30 min are allowed within an event to account for thin, patchy cirrus clouds advecting over the SGP site). This assumes that criterion #2 is already met.
   b. When reflectivity measurements extend from the threshold height (determined in step 1) to 2 km above the threshold height. In this case, all reflectivity measurements occurring within ±30 min are excluded from the cirrus cloud mask.

Part b of step 3 in the above criteria is essential to excluding cloud events that could be mistaken for deep convection or very thick midlevel clouds.

Figure 1a shows MMCR reflectivity measurements for 24 h (in UTC time) on 3 June 2009. A thick cirrus cloud is observed from around 02:30 to around 14:00 UTC, and later a shallower cirrus cloud is measured from just before 16:00 to after 24:00. Figure 1b demonstrates how two cirrus cloud events (red mask) were identified: both cirrus events were separated by over 1 h while remaining above the height threshold determined in step 1 of the prescribed algorithm. All reflectivity measurements below the height threshold have a blue mask and are excluded as candidate cirrus cloud cases for study. In this example and for all other candidate cases, the cirrus event definition allows for easier and clearer matching with radiosonde observations while providing additional metadata (e.g., cirrus event duration) for interpreting the results involving the atmospheric state classifications of cirrus cloud RHI. Overall, there are 2267 cirrus cloud events identified from our analysis (averaging to ~0.9 cirrus events per day), including the two events presented in Figure 1.

At this step, radiosonde data are incorporated into the analysis. The first challenge is ensuring that the radiosonde measurements are collocated with the appropriate MMCR measurements. When a radiosonde is

launched, it can take a half hour or more to reach altitudes above 6 km. Also, horizontal wind speeds below 3 km are considerably slower (i.e., ~10 m/s) than those wind speeds in the middle and upper troposphere (i.e., ~20 m/s or greater). Thus, a cirrus cloud sampled at the instant the radiosonde is launched will initially travel farther downwind than the radiosonde. For this reason, we imposed a "lag time" on the radiosonde measurements, which is computed as the following:

$$\Delta t = \frac{z_{\text{cloud}}}{\text{mean}\left(\frac{\Delta z}{\Delta t}\right)_{\text{sonde}}} \tag{3}$$

where z_{cloud} is the median cirrus cloud event height and $\text{mean}(\Delta z/\Delta t)_{\text{sonde}}$ is the mean radiosonde ascent rate from ground level to the median height of the cirrus cloud event. This time is subtracted from the radiosonde launch time to best approximate when the radiosonde and MMCR measure roughly the same altitude (over the same place). The aforementioned methodology is presented with reasonably high confidence: given that the majority of cirrus cloud events last longer than an hour, radiosondes can fully measure a cirrus cloud before the event ends provided that the radiosonde is launched far enough in advance to the end of the event. We tested the sensitivity of our results to this lag time for $\Delta t \pm 10$ min and found that our results did not significantly change. This is especially important for radiosonde observations in "patchy" cirrus cloud events, where a short time difference could result in the radiosonde ascending through clear skies instead of the intended cirrus cloud. Therefore, it is reasonably safe to assume that for the short time periods (i.e., ~1 h), the radiosonde (once it rises above the boundary layer) and the cirrus cloud will travel at approximately similar speeds and in a very similar direction. Under this assumption, the radiosonde will ascend through the sampled cirrus cloud.

To verify the matching of cloud boundaries between the radiosonde and MMCR data, we computed the average distance between the cirrus cloud top altitudes that were computed using two distinct methods:

1. The cloud top altitude is the highest altitude with significant reflectivity observed by the MMCR.
2. The cloud top altitude is the height where the RHI is the largest in the profile, since the highest RHI in cirrus clouds are typically observed near the cloud top.

We found that the median difference between the two estimates was 50 m, with the RHI-estimated cirrus cloud top being lower than the uppermost significant echo from the MMCR. Because this difference falls within the range resolution of the MMCR, we believe that the MMCR and radiosonde are accurately collocated at the cloud top.

Verifying the radiosonde/MMCR matching at cloud base, however, is more challenging. Reflectivity measurements at cloud base are almost always indicative of precipitating ice crystals falling into subsaturated air; thus, discerning a clear-air layer from a precipitating ice crystal layer is not possible with the data sets used in this study. However, we show later that RHI measurements less than 60% occur 20–35% of the time, a result that is consistent with the RHI statistics shown in *Comstock et al*. [2004], which used perfectly collocated and validated measurements of water vapor and backscatter from Raman lidar in cirrus clouds. Thus, we feel that our results, which are statistics derived from hundreds of cases, have relatively small mean sampling error despite the inherent limitation and challenge of collocating the radiosonde and MMCR measurements.

In addition to ensuring the best possible collocation between the radiosonde and MMCR measurements, the cloud itself must be screened to ensure that it is composed entirely of ice. An MMCR observation is considered a cirrus event if it passed the previous altitude and longevity requirements *and* all RH (with respect to water) measurements taken inside the cirrus cloud are less than 95%, thereby eliminating any liquid or mixed-phase clouds.

Figure 2 shows the profiles of RHI collocated with Figure 1. In Figures 2a and 2b, the radiosonde is ascending through a cirrus cloud deck approximately 4 km in depth. At the base of the cloud indicated in Figures 2a and 2b, the MMCR is measuring portions of the cirrus cloud in an evidently dry layer (between 8 and 9 km) while RHI nears ~110% near the top of the cloud. The structure of RHI between Figures 2a and 2b, however, varies through the middle of the cloud. Specifically, a layer of subsaturated RHI exists between 10 and 11.5 km in Figure 2b, whereas RHI steadily increases from 9 to 12 km in Figure 2a. Patchy cirrus with clearly observable fall streaks are evident in the second cirrus event on this day (Figures 1 and 2d). In particular, the RHI is subsaturated in the bottom and middle portions of the cloud (Figure 2d) and supersaturated near the top, where RHI sharply decreases just above the MMCR-observed cloud top and becomes supersaturated again. Figure 2d highlights

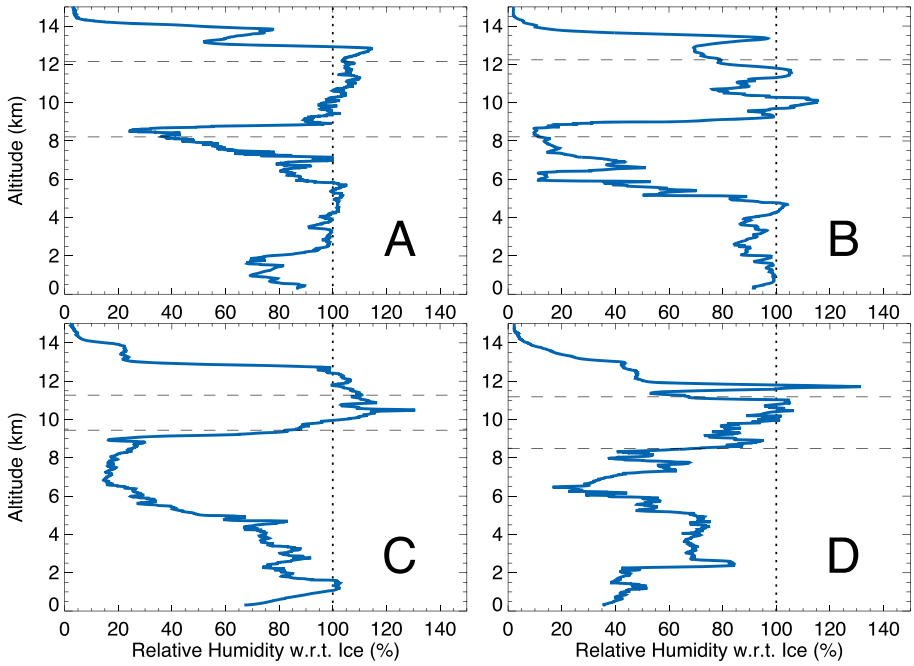

Figure 2. Profiles of RHI derived from SGP radiosondes at (a) 05Z, (b) 11Z, (c) 17Z, and (d) 23Z for 3 June 2009. Each radiosonde, using the algorithm described in the text, was collocated with cirrus cloud event 1 or 2 shown in Figure 1. The launch times were adjusted for time lag according to equation (3). The horizontal dashed lines indicate the collocated cloud boundaries.

the variability in RHI that is observed in patchy cirrus—especially during the summer when the atmosphere is generally less active at the SGP site.

Using our definition of a cirrus cloud event, 1076 cases (i.e., cirrus cloud events) were identified and are included in the analysis. The sampled cirrus clouds (within the defined cirrus events) have an average geometric thickness of 1.74 km, which is a bit shallower than the 2.0 km thickness reported in *Mace et al.* [2001]. Cirrus clouds generally reside between 8 and 10 km from October to April, while cirrus clouds often occur between 10 and 12 km from May to September (Figure 3). Additional statistics of the radiosonde-sampled cirrus clouds are presented in Table 1 (the atmospheric state classifications are described in the next section). It should be noted that the altitude of cirrus cloud tops might be underestimated by the MMCR measurements [*Borg et al.*, 2011], and therefore, the cloud top altitude and temperature, as well as cirrus cloud thickness, statistics in Table 1 may be slightly low biased. This limitation is especially important for optically thick clouds, because this bias is more likely to be observed in thick cirrus (some evidence of this bias is seen in Figures 2a and 2c, where the measured cloud top is lower than the height of the supersaturated RHI layer). We will address this caveat in section 2.5.

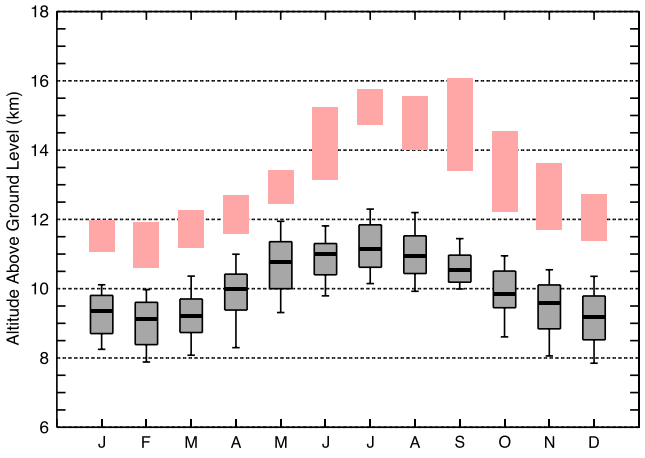

Figure 3. The median altitude (measured from the center of individually sampled cirrus clouds) of cirrus clouds versus month of year. The 10th through 90th percentile of data is represented in each box-and-whisker plot. The red rectangles above each box-and-whisker plot represent the 25th through 75th percentile of tropopause height for that month, where tropopause height was derived from the radiosonde data.

Table 1. Basic Statistics of the Radiosonde-Sampled Cirrus Clouds (1076 Total) for the 7 Year Period From January 2004 to January 2011[a]

	Number of Samples (% of Total)	Cirrus Event Duration (Hours)	Cloud Base Altitude (km)	Cloud Top Altitude (km)	Cloud Thickness (km)	Cloud Base Temperature (C)	Cloud Top Temperature (C)
Summer	347 (32.2)	1.8 ± 2.8	10.0 ± 1.0	12.0 ± 1.1	1.7 ± 1.1	−36.8 ± 7.4	−52.8 ± 7.7
Anticyclone	125 (11.6)	2.0 ± 2.9	8.9 ± 1.0	10.6 ± 1.1	1.8 ± 1.0	−38.2 ± 6.9	−53.7 ± 5.9
Cold front	159 (14.8)	1.8 ± 2.8	8.6 ± 1.3	10.7 ± 1.5	1.9 ± 1.1	−35.7 ± 7.4	−52.3 ± 7.7
Southerly	294 (27.3)	2.2 ± 3.1	8.8 ± 1.1	10.9 ± 1.2	1.7 ± 1.2	−38.1 ± 7.9	−54.9 ± 6.9
Northerly	151 (14.0)	1.6 ± 2.6	8.4 ± 1.3	10.0 ± 1.4	1.4 ± 1.0	−36.8 ± 7.1	−49.1 ± 6.8

[a]All data are represented as the median ±1 standard deviation.

2.4. Atmospheric State Classification Algorithm

The cirrus cloud events are grouped into atmospheric state classifications as defined by *Marchand et al*. [2009]. In their study, *Marchand et al*. [2009] used a self-organizing map neural network (i.e., pattern recognition) algorithm to define a set of atmospheric states for a domain centered over the ARM SGP site. The algorithm ingested 3 years of Rapid Update Cycle as input, resulting in 12 unique atmospheric states. The algorithm was updated in 2012 [*Evans and Marchand*, 2013] to utilize 13 years (from 1997 to 2010, at 6 h time intervals) of ECMWF ERA-Interim reanalysis data and ARM Ka-band radar data. The updated algorithm resulted in 21 atmospheric state classifications, which are grouped into five parent classifications. Considering that our study involves upper tropospheric cirrus, the five parent classifications and their typical upper tropospheric characteristics are as follows:

1. *Anticyclone* (*Marchand et al*. *states 1*, *7*, *and 13*). An upper level ridge is centered over the domain (with westerly/northwesterly flow in the middle/upper troposphere) and is accompanied by a surface anticyclone.
2. *Southerly* (*Marchand et al*. *states 4*, *5*, *8*, *and 17*). A southerly or southwesterly flow regime dominates over the domain (near the surface and in the middle/upper troposphere).
3. *Cold front* (*Marchand et al*. *states 12*, *14*, *18*, *and 20*). These states represent the progression of a cold front across the domain, including two-prefrontal, a postfrontal, and frontal-passage subclassifications.
4. *Northerly* (*Marchand et al*. *states 2*, *6*, *16*, *19*, *and 21*). Strong surface northerly winds become westerly/northwesterly with height and typically follow cold front states.
5. *Summer class* (*Marchand et al*. *states 3*, *9*, *10*, *11*, *and 15*). These states are warmer than the other 16 Marchand et al. atmospheric states and typically have near-surface southerly winds becoming westerly with height.

Further detail about the atmospheric state classification algorithm and updated atmospheric states can be found in *Marchand et al*. [2009] and *Evans and Marchand* [2013]. In cases where a cirrus cloud lasts longer than 6 h (which occurs approximately 15–20% of the time, depending on the classification), RHI data are binned according to the atmospheric state at radiosonde launch time.

2.5. Analysis Techniques

This study quantifies RHI and other variables as a function of the five parent classifications, which generalize the atmospheric states dynamically and thermodynamically. However, analysis from individual subclassifications will complement this study where appropriate because certain characteristics among states within a parent class do vary considerably. For brevity, we will use "atmospheric states" or "classes" throughout the rest of this paper to refer to the five parent classifications and *not* the 21 individual atmospheric states comprising their respective parent classifications. Seasonal analyses of RHI are also shown to contextualize the atmospheric state classification analyses because each class is at least somewhat dependent on seasonality (Table 2).

Previous studies have shown that the greatest frequency of saturated RHI measurements occurs near the top of the cloud [*Heymsfield and Miloshevich*, 1995; *Comstock et al*., 2004]. Following the methodology described in *Comstock et al*. (2004), we characterize the vertical distribution of RHI in cirrus clouds by using the median value in the top 25%, middle 50%, and bottom 25% of the cloud. Emphasis will be placed on the top 25% and bottom 25% regions because, in general, the maximum RHI measured within cirrus clouds occurs near the top of the cloud (Figure 4) and RHI near the base of the cloud can proxy the likelihood of sublimating/evaporating ice crystals.

Table 2. The Number of Cirrus Cloud Cases to the Number of Clear-Sky Scenes for Each Season (Winter, Spring, Summer, Fall, and All Seasons From Left to Right) With the Percentage of Cirrus Cloud Cases (to the Total Number of Cirrus Cloud and Clear-Sky Cases) Shown in Parentheses[a]

Classification	DJF	MAM	JJA	SON	All Seasons
Summer	NA	31/63 (33.0%)	266/360 (42.5%)	50/79 (38.8%)	347/502 (40.9%)
Anticyclone	47/83 (36.2%)	39/105 (27.1%)	NA	27/58 (31.8%)	125/252 (33.2%)
Cold front	45/93 (32.6%)	61/129 (32.1%)	NA	37/78 (32.2%)	159/325 (32.9%)
Southerly	89/84 (51.4%)	139/181 (43.4%)	NA	59/86 (40.7%)	294/356 (45.2%)
Northerly	79/205 (27.8%)	40/113 (26.1%)	NA	22/69 (24.2%)	151/413 (26.8%)

[a]The number of clear-sky scenes was determined using radiosonde and MMCR data over the specified time period, where RHI measurements less than 95% and no reflectivity measurements over −35 dB*Z* constituted a clear-sky scene. Seasons where fewer than 30 observed (combined) cirrus clouds or clear-sky scenes are not shown. DJF: December-January-February. MAM: March-April-May. JJA: June-July-August. SON: September-October-November. NA: not available.

For the majority of our analyses, we chose to aggregate data according to the state classification and cloud region. One caveat to aggregating data in this fashion is that thick cirrus clouds (greater than 3 km in depth) have a greater number of points per sample compared to thin cirrus clouds (i.e., less than 1 km in depth). For example, a 3 km thick cloud sampled at 10 m vertical resolution will have 300 points, whereas a 1 km thick cloud at the same vertical resolution will have 100 points. By contrast, the number of points sampled by the MMCR for each case would be ~30 and 10 points, respectively. To avoid biasing our results toward thick clouds, we normalized all profiles (from the radiosonde and MMCR) to a 100-point profile. Although this number is somewhat arbitrary, we chose this number because it maintains the structure of the original profile for all clouds (i.e., maximum and minimum values and shape of profile). Our results are not sensitive to the number of points in the normalized profiles (not shown). Finally, for the majority of the analyses, results are shown as box-and-whisker plots from the 10th to 90th percentiles. Normalizing data profiles and aggregating them as described means, for example, cloud base and cloud top RHI are shown such that each radiosonde-sampled cirrus cloud contributes 25 points to the aggregated data set.

As pointed out in *Borg et al*. [2011], the MMCR can underestimate the altitude of the top of a cirrus cloud especially if there are small particles at the top of the cirrus layer. By not observing the top of the cirrus, significant outgoing longwave flux biases of about 16 to 20 W m^{-2} can occur [*Borg et al*., 2011; *Protat et al*., 2014], while some biases are as large as 100 W m^{-2}. The underestimation in geometric depth, however, is usually no more than a couple hundred meters [e.g., *Sassen and Khvorostyanov*, 1998]. Because the top region of the cloud is generally where new ice crystal nucleation takes place (and hence where RHI tends to reach peak saturation), we also analyze RHI *above cloud*. We define "above cloud" as the depth extending 180 m from the measured cloud top, where 180 m is analogous to two MMCR range gates (recall that the vertical resolution of the MMCR Mode 2 data is 90 m). To clarify, our definition of above cloud accounts for RHI that is *likely* within the cirrus cloud layer but, due to the MMCR's measuring limitations, was identified at an altitude(s) where the MMCR did not detect a cloud.

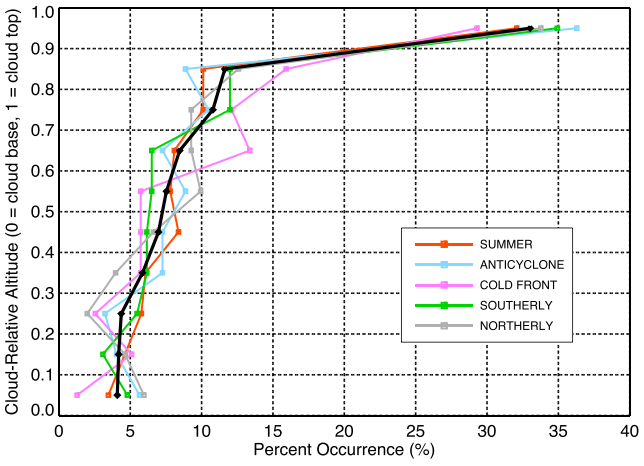

Figure 4. Median profiles showing the occurrence of maximum RHI relative to the depth of the cloud in which the maximum RHI was measured. The colored lines denote profiles for specific classifications, while the superimposed thick black line shows the median for all cases (1076 cases total; refer to Table 1 for the number of cases in each profile).

We further investigate the potential for new cirrus cloud growth by analyzing clear-sky RHI as a function of atmospheric state. Radiosonde observations that occur during a period when the MMCR does not measure any reflectivity echoes greater than −35 dB*Z* through the duration of the radiosonde's flight time are considered a clear-sky scene.

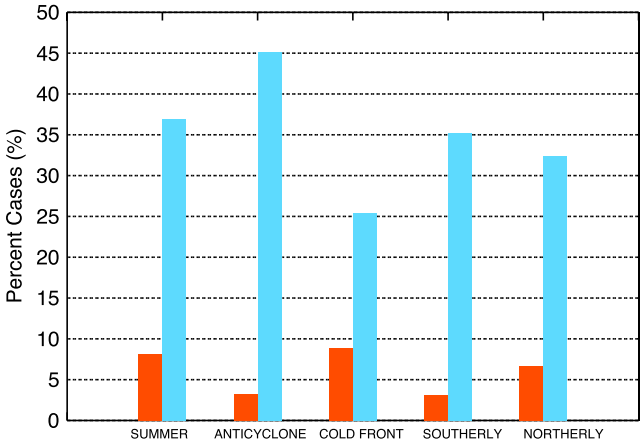

Figure 5. The percentage of cirrus clouds existing in temperatures entirely warmer than −40°C (red) and entirely colder than −40°C (blue).

For all available cirrus cloud cases (1076 total), a Monte Carlo sampling technique is applied to analyze clear-sky RHI. The steps to this technique are as follows:

1. For a given cirrus cloud, a clear-sky sounding with the same atmospheric state classification is *randomly* selected.
2. A subset of RHI measurements (from the same altitudes as the cirrus cloud) is taken from the clear-sky sounding.
3. The subset data are further parsed into the bottom 25%, middle 50%, and top 25% regions, analogous to the measured cirrus cloud.
4. The median RHI from the respective regions is recorded and grouped into the appropriate classification.

One important discussion point in this study is the relevance of our results to the uncertainty in the measurements. Since RHI is a function of both RH and temperature, we computed uncertainty in RHI using the total uncertainty for radiosonde temperature ($\Delta T = 0.5$°C) and RH ($\Delta \mathrm{RH} = 5\%$) in the following root-mean-square error formula (following *Immler et al.* [2010, equation 2]):

$$\Delta_{\mathrm{RHI}} = \sqrt[2]{[\mathrm{RHI}(T,\mathrm{RH}) - \mathrm{RHI}(T+\Delta T,\mathrm{RH})]^2 + [\mathrm{RHI}(T,\mathrm{RH}) - \mathrm{RHI}(T,\mathrm{RH}+\Delta \mathrm{RH})]^2} \quad (4)$$

In general, total RHI uncertainty is approximately 7.0–7.5% in the cloud base region, 8.0–8.5% in the cloud top region, and between 8.0 and 9.0% above the cloud top region. Daytime RHI measurements, which were corrected for the solar radiation-induced dry bias using *Wang et al.* [2013], are subject to an additional 2% uncertainty due to the uncertainty in the quantities hf (heating factor; accounts for the heating of the RH sensor relative to the temperature sensor) and cf (adjustment factor; accounts for cloud coverage) that are a part of the correction equation (additional details are given in *Wang et al.* [2013]). Despite this additional uncertainty, there are no significant differences in our results when evaluating them diurnally (result not shown). Finally, the uncertainty in RHI does not vary significantly among the five classes.

3. Results and Discussion

The thermodynamic environments among the five classifications vary considerably, thus influencing the RHI. Approximately 94% of all cirrus clouds observed in this study had at least a portion of the cloud that was colder than −40°C, but among the classifications, the percentage of cirrus clouds that were entirely colder than −40°C varies considerably (Figure 5). The anticyclone class contains the highest percentage of cases where the entire cirrus clouds were entirely colder than −40°C, whereas the cold front class has the lowest percentage.

This is also reflected in the percentage of cirrus cloud cases from the five classifications where the highest RHI exceeded 140% (Table 3). In the anticyclone class, 3.2% of all sampled cirrus clouds had a maximum RHI

Table 3. The Percentage of Cirrus Clouds in Each Parent Classification Where RHI Exceeds 100%, 120%, and 140%

Classification	Percent of Cases Where RHI > 100%	Percent of Cases Where RHI > 120%	Percent of Cases Where RHI > 140%
Summer	71.4%	21.7%	1.4%
Anticyclone	78.2%	29.0%	3.2%
Cold front	74.5%	24.8%	0.6%
Southerly	76.1%	29.5%	1.4%
Northerly	71.5%	25.8%	1.3%

Table 4. Median RHI (in %) for the Cloud Bottom, Middle (Bolded), and Top Regions (From Left to Right) as a Function of Season and Atmospheric State[a]

	DJF	MAM	JJA	SON
Summer	NA	74.9, **85.9**, 101.4	76.5, **93.5**, 103.4	81.4, **104.7**, 114.1
Anticyclone	89.2, **98.0**, 104.7	80.7, **98.9**, 113.1	NA	82.0, **99.2**, 109.3
Cold front	79.0, **95.8**, 106.1	89.3, **96.6**, 110.6	NA	85.7, **97.1**, 105.1
Southerly	93.2, **103.7**, 115.4	79.7, **94.2**, 108.4	NA	78.6, **96.7**, 109.1
Northerly	88.1, **98.0**, 109.5	78.0, **91.0**, 109.4	NA	86.1, **100.7**, 115.6
All states	88.7, **99.3**, 110.3	80.7, **94.1**, 108.8	76.5, **93.8**, 104.1	83.1, **98.6**, 109.9

[a]The seasonal median RHI for the cloud bottom/middle/top regions is given in the bottom row. Seasons where fewer than 30 observed (combined) cirrus clouds or clear-sky scenes are not shown.

exceeding 140%, while maximum RHI in the cold front class exceeded 140% only 0.6% of the time (Table 3). Although we do not explicitly resolve ice nucleation mechanisms in this study, these statistics of temperature and RHI agree with the results presented in *Cziczo et al*. [2013]. As pointed out by *Mace et al*. [2006], however, cirrus clouds measured by the MMCR are likely generated several kilometers upstream of the measurement location; thus, we cannot make definitive statements relating classifications, RHI, and ice nucleation. Regardless, even though a very small percentage of cirrus clouds observe RHI greater than 140%, ice supersaturation occurs between 70 and 80% of the time depending on the classification (Table 3).

The frequency in which a classification occurs is at least somewhat tied to the annual cycle, which means that the thermodynamic regimes characteristic of each classification are dependent on season. Table 4 reveals a seasonal trend in cirrus cloud RHI: a minimum in RHI (for all three cloud height regions) is observed during the summer months, whereas a maximum occurs in the winter months. When comparing the middle and bottom regions of cirrus clouds during the spring and fall, slightly higher RHI (~4%) is observed in the fall. Median cirrus cloud RHI for each month of the year is shown in Figure 6 and shows how monthly variations in cirrus cloud RHI evidence seasonality (note that a similar result was found when using maximum RHI instead of median RHI, but this is not shown). The seasonal trend in cirrus RHI does not necessarily correlate with overall cloud occurrence; based on our sampling, we observe more cirrus clouds during the summer compared to the winter (310 to 258 cases, respectively), and more cases are observed in the spring compared to the fall (307 to 195 cases, respectively). These observations are consistent with *Mace et al*. [2006] where a minimum in cirrus cloud occurrence was observed in the late summer/early fall (i.e., September) and an observed increase in cirrus occurrence began in March. *Wylie et al*. [1994] also found an increased occurrence of cirrus clouds in the summer compared to the winter. Overall, the link between cirrus cloud occurrence and RHI observed within cirrus clouds is somewhat contradictory and therefore not entirely explained by seasonal thermodynamic regimes.

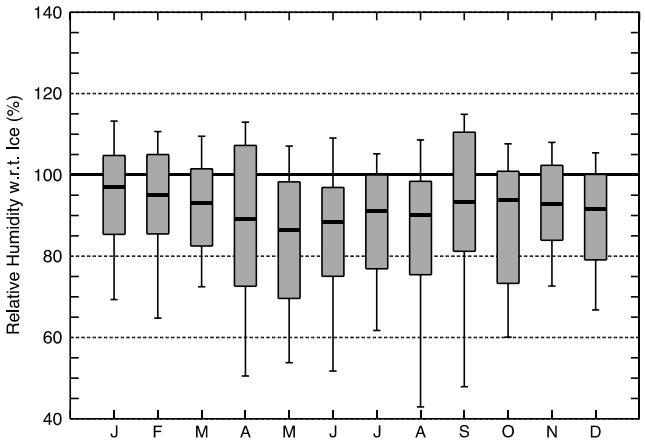

Figure 6. Box-and-whisker plots (10th through 90th percentile) of median cirrus cloud RHI for each month of the year (January through December, left to right).

In the winter months, RHI through the depth of cirrus clouds is highest compared to any other season (Table 4). We also find an increased percentage of cirrus cloud scenes compared to clear-sky scenes (Table 2) in the winter months versus any other season. The southerly class stands out as having both the highest frequency of cirrus clouds relative to clear-sky scenes (51%) and the highest RHI in every cloud region for the winter, where both the middle and top regions have a median RHI exceeding 100%. These observations suggest that the dynamical and thermodynamical regimes represented in the southerly class are most conducive for wintertime cirrus formation.

For example, the jet stream (often represented in the southerly classification) [*Muhlbauer et al*., 2014] is strongest over the continental U.S. during the wintertime. Vertical motions induced at the entrance/exit regions of a jet streak are stronger, and given that the midlatitude atmosphere is driest during the winter, stronger upward vertical motion would induce faster adiabatic cooling [*Spichtinger et al*., 2005] and therefore higher observed RHI values. Cirrus clouds are more likely to occur in the winter as a result of midlatitude cyclones and jet streams compared to the summer [*Mace et al*., 2001].

There is a caveat to the wintertime median RHI through the cloud depth: all nonsoutherly class cirrus has RHI (with one exception for one region) below the seasonal median values for the three cloud height regions. We suspect that because southerly class cirrus account for 34% of all wintertime cases, the (statistically higher) RHI weights the seasonal RHI median values higher. Dynamically, the southerly class is most similar to the cold front class; however, RHI is generally smaller through the depth of the cloud likely because the atmosphere is overall warmer (Table 1 and Figure 5). This reasoning is consistent with *Mace et al*. [2006] where they found that cirrus most often occurs in regions of maximum RH downstream of maximum vertical motion—a description analogous to a southerly state [*Evans and Marchand*, 2013]. We conclude, for wintertime cirrus, that new cirrus formation is especially favorable in the southerly class because the characteristic thermodynamic and dynamical regimes stimulate vertical motions (i.e., adiabatic cooling) that lead to high values of RHI.

Median cirrus cloud RHI is higher for all cloud regions in the fall compared to the spring, but there is considerable RHI variability among the classifications comprising each season. Unlike the winter season where southerly cirrus has the highest overall observed RHI, cirrus in the anticyclone class has the highest median RHI for the middle and top regions in the spring. Despite having similar thickness, cloud base and top temperature, and cloud base and top altitude (Table 1), cirrus still form more frequently in the southerly class compared to the anticyclone class (43% to 27%; see Table 2). A similar phenomenon is observed in the fall: median RHI is higher in each cloud region for anticyclone class cirrus compared to southerly class cirrus (although the RHI difference between each region does not exceed 4%) even though a higher frequency of cirrus is observed in the southerly class (41%) compared to the anticyclone class (32%). The dynamical regimes characterizing the anticyclone and southerly classes are nearly opposite; upper level large-scale subsidence occurs in the anticyclone class, whereas large-scale rising motions occur in the southerly class. According to *Evans and Marchand* [2013], subclass 13 of the anticyclone class differs from the other two subclasses because moisture is found overrunning the upper level ridge over the SGP site. In our study, cirrus from subclass 13 accounts for 45% of the cirrus in the anticyclone class and RHI from this subclass is generally 2–5% higher on average compared to the other two subclasses (result not shown). This information explaining the high RHI values found in the anticyclone class, coupled with the characteristic dynamical regime of the southerly class, suggests that favorable dynamical environments (as opposed to regions of high RHI) are more responsible for cirrus cloud occurrence.

This hypothesis is further corroborated by cirrus cloud RHI from the northerly class. When comparing the anticyclone and southerly classes to the northerly class, we find the values of RHI in the northerly class to be slightly less overall although this difference is not statistically significant (Figure 7). Cirrus occurrence in the northerly class is the lowest (27%) compared to all other classifications (Table 2). Similar to the anticyclone class, the environmental dynamics associated with the northerly class are unfavorable for cirrus cloud development. A northerly state typically follows a cold front state [*Evans and Marchand*, 2013], which implies that an upper level ridge (which promotes rising surface pressure) builds in over the SGP site. Thus, many cirrus clouds observed in the northerly class are likely residual (dying) clouds from a cold front state (more evidence of this process will be presented later). Another important note involves above-cloud RHI: this quantity does not vary significantly among the anticyclone, southerly, and northerly classes even though northerly class cirrus clouds are statistically thinner and have shorter lifetimes compared to the other classes (Table 1). We conclude, based on this result, that our statistics of RHI in the cirrus cloud top region are unaffected by the MMCR's low cloud top altitude bias described in *Borg et al*. [2011] and *Sassen and Khvorostyanov* [1998].

Summer class cirrus clouds are unique from cirrus in the nonsummer classes due to their statistically lower observed values of RHI but generally high rate of occurrence (41%). Cirrus clouds forming in the summer class are less likely to form from synoptic-scale weather systems; if anything, localized convective towers (analogous to "pop-up" thunderstorms or something similar) are responsible for most dynamically induced cirrus

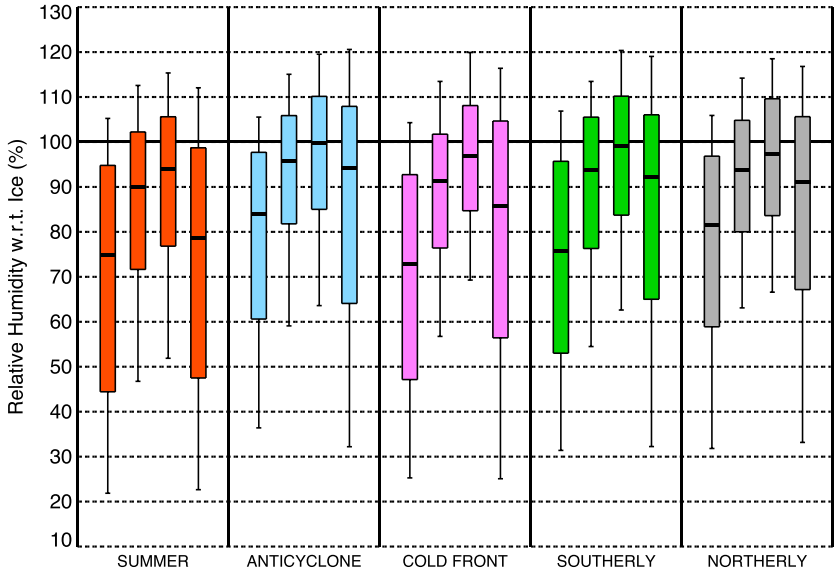

Figure 7. Box-and-whisker plots (10th through 90th percentile) of RHI in the bottom 25% region (far left), middle 50% region (middle-left), and top 25% region (middle-right) of sampled cirrus clouds, along with above-cloud RHI (far right), for the five parent classifications.

formation. Otherwise, cirrus events in the summer class are mostly patchy and evidenced by the shorter time duration (~1.8 h; see Table 1) compared to the southerly and northerly classes. Despite the lack of large-scale vertical motions in the summer state, what explains the higher rate of cirrus occurrence? *Kärcher et al.* [2014] used a Large Eddy Simulation model to demonstrate differences in cirrus macrophysical properties when accounting for slow (weakly damped RHI fluctuations) and fast (strongly damped RHI fluctuations) uptakes of water vapor by ice crystals. Their results showed that RHI is generally lower when fast water vapor uptake by ice crystals occurs but that RHI could be maintained if there is upward vertical motion of at least 4 cm/s. Given that the summer classification is overall less dynamically active compared to the other classifications, the work presented in *Kärcher et al.* [2014] offers at least one plausible hypothesis explaining why summer cirrus has statistically lower RHI. Another explanation could be potential radiosonde/MMCR mismatching because of the larger number of patchy cirrus cloud cases in this classification.

Our analysis thus far has covered cirrus RHI and how this quantity varies in thermodynamic (seasonal) and dynamical (atmospheric state) regimes; however, variability in cirrus cloud RHI is observed when accounting for cloud (geometric) thickness (Figures 8a1–8a3). For thin cirrus clouds, median observed RHI is ~70–80% at the cloud base and ~90–100% near the cloud top (Figure 8a1). Thick cirrus clouds, by contrast, have median observed RHI values of 45–80% near the cloud base and 85–105% near the top of the cloud (Figure 8a3). Variability in median reflectivity measurements for different synoptic classifications is also observed for thicker cirrus clouds (Figures 8c1–8c3); this finding corroborates with *Mace et al.* [2001], where greater macrophysical variability was observed in thick cirrus clouds compared to thin cirrus clouds. Using reflectivity as a proxy, we also see macrophysical variability among the five classifications. Figure 8c3, for cirrus clouds thicker than 3 km, shows that the highest median reflectivity values are observed for cold front cirrus followed closely by northerly cirrus. Recall that a northerly class generally follows a cold front class, and given the dynamical regimes associated with a northerly class, cirrus in this class likely formed in a cold front class and are thus likely clouds in the decaying phase of their lifecycle (recall that cirrus in the northerly class is statistically thinner from the other classes). Both of these classes have cirrus clouds forming in slightly warmer environments compared to the southerly and anticyclone classes (Table 1), therefore leading to higher median ice water content (IWC; result not shown). *Mace et al.* [2001] explained that IWC tends to scale exponentially with higher temperature, thus corroborating our results. For clouds thicker than 3 km, Figure 8b3 reveals a moisture inversion at the base of northerly cirrus clouds, and Figure 8a3 shows lower median RHI through the depth of this cirrus for this class compared to the other four classes. Overall, this evidence supports the idea that northerly class cirrus is indeed residual cold front class cirrus.

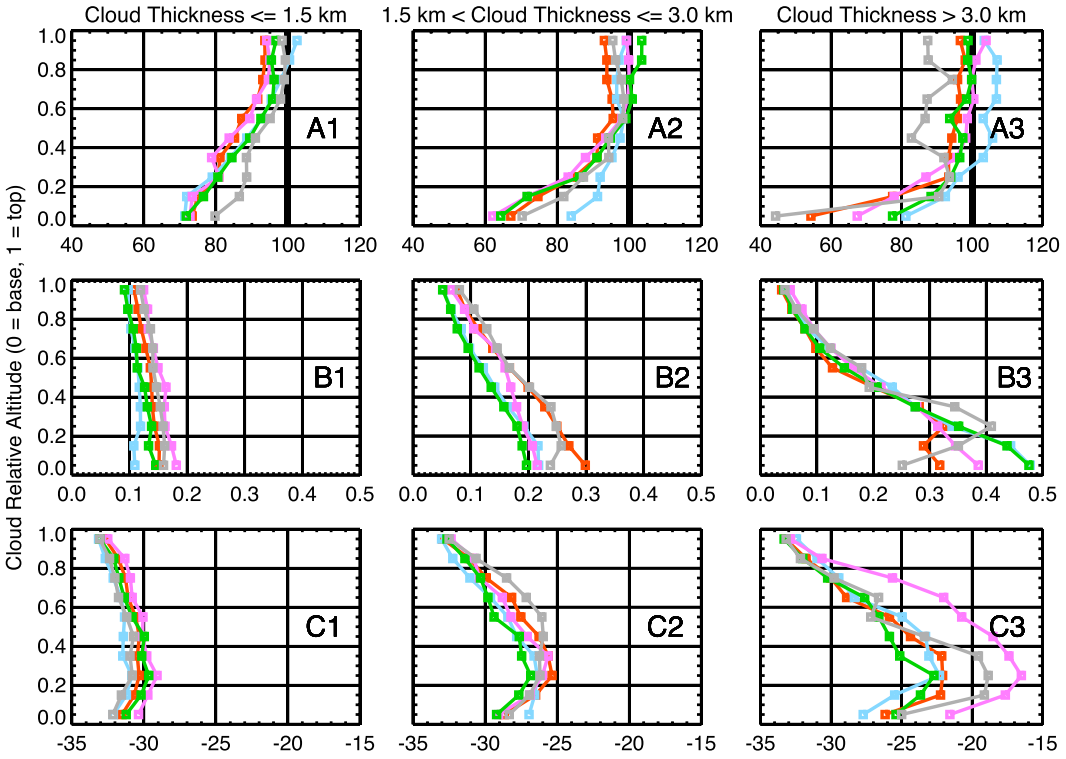

Figure 8. Profiles of (a1–a3) median RHI (in %), (b1–b3) water vapor mixing ratio (in g/kg), and (c1–c3) reflectivity (in dBZ) normalized by cloud depth (0 represents the cloud base, and 1 represents the cloud top). The vertical bin spacing is 0.1 altitude units (i.e., there are 10 bins). The summer, anticyclone, cold front, southerly, and northerly classes are represented by the colors red, blue, purple, green, and gray, respectively.

Using the Monte Carlo sampling technique described in section 2.5, we find substantial differences in RHI under clear-sky conditions (Figure 9). Clear-sky RHI is highest overall in the anticyclone and southerly classes, which follows previous results showing that RHI is particularly high in these two classifications. Clear-sky RHI in the cold front state is lowest overall, likely because a majority of the clear-sky cases observed for a cold

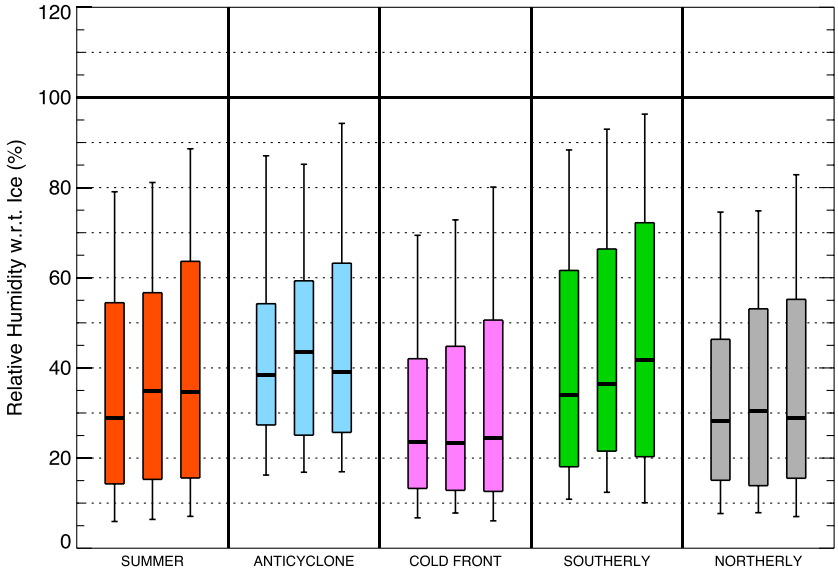

Figure 9. Box-and-whisker plots (10th through 90th percentile) of RHI measured in clear-sky scenes using the Monte Carlo sampling technique described in the text.

front class are postfrontal. Summertime clear-sky RHI is also particularly low, though the computed interquartile ranges are larger compared to the cold front class. Overall, given that the southerly and anticyclone classes have the highest overall clear-sky RHI, we suspect that these two classes—compared to the other two classes—are better able to support new cirrus cloud development and maintenance.

4. Conclusions and Future Work

In this study, a seasonal dependence is found for cirrus cloud RHI, where maximum RHI is observed during the winter and minimum RHI is noted for the summer. When accounting for seasonality and atmospheric state, cirrus cloud RHI varies considerably. In most cases, the variations in RHI (among the prescribed cloud regions) are within the measurement uncertainty and only the summer class has statistically lower RHI compared to the other classes. The magnitude of the observed RHI in cirrus clouds is not correlated with overall cloud occurrence frequency, as was noted in this study and in previous studies such as *Wylie et al*. [1994] and *Mace et al*. [2006]. The southerly class stands out as having the highest overall RHI in cirrus clouds, likely because the thermodynamic and dynamical regimes characterizing this class favor both high RHI and increased cirrus cloud occurrence. Cirrus cloud RHI is not statistically different among the nonsummer classes, however, though we find that cirrus in the anticyclone has consistently high RHI as well. We therefore speculate that for cirrus clouds forming in dynamically unfavorable environments, higher overall RHI compensates for the lack of dynamics that would otherwise favor new cirrus cloud development. We suspect that the lower frequency of cirrus in the winter, relative to the summer, is because more atmospheric states characterizing the winter have dynamical regimes unfavorable for new cirrus cloud development (i.e., anticyclone and northerly classes). Overall, our results support previous studies such as *Mace et al*. [2006], *Berry and Mace* [2013] and others showing that large-scale dynamical regimes are most important to explaining variability in cirrus cloud macrophysical and microphysical properties.

Using our results, we hope that future studies can provide additional insight linking cirrus cloud occurrence to RHI for a midlatitude site. We feel that this is especially important for summertime cirrus; although a high frequency of cirrus clouds is observed in the summer class, the reason that this occurs—especially when accounting for RHI—is not fully understood. One hypothesis could be that during the North American monsoon (which takes place during the summer), cirrus is more easily formed in the eastern Pacific Ocean and advected over the SGP site (we note that based on the radiosonde data, 48% of the cirrus observed in the summer class advected from the southwest, compared to 34% from the northwest). Low RHI due to strong water vapor diffusion onto newly forming ice crystals, as discussed in *Kärcher et al*. [2014], is one plausible explanation. Regardless, the lack of definitive results for the summer class is at least partly manifested in the fact that midlatitude cyclones and overall weak disturbances are binned in the summer class because geopotential heights are very high—thus generalizing this classification more on thermodynamic regimes compared to dynamical regimes. Therefore, further work on this subject will employ a more detailed atmospheric state classification of the SGP site, such as the scheme outlined in *Kennedy et al*. [2015], which also used the methodology of *Marchand et al*. [2009].

For midlatitude locations such as the ARM SGP site, a vast number of processes occur that influence the occurrence of cirrus clouds and their macrophysical/microphysical properties. At this time, we cannot reasonably conclude that variations in RHI for the different synoptic classifications are the primary driver of the differences in cirrus cloud properties among the classifications, especially since the majority of the RHI results do not exceed the computed measurement uncertainties.

Acknowledgments
The authors would like to thank Cameron Homeyer for providing the code needed to compute tropopause height from the radiosonde data. The authors would also like to thank Steven Cavallo and David Parsons for their input on the original work leading to this paper. Finally, the authors would like to thank Robert Rabin, Ariel Cohen, and five anonymous reviewers for their suggestions and comments that have greatly improved the clarity and quality of this manuscript. This work was supported by the U.S. Department of Energy's Atmospheric System Research (ASR) program with grant DE-SC0008830. The radiosonde and MMCR data used in this study were downloaded from the ARM program's data archive at archive.arm.gov. Stuart Evans graciously provided the classification data used in this study.

References

Ackerman, T. P., and G. M. Stokes (2003), The Atmospheric Radiation Measurement program, *Phys. Today*, *56*, 38.
Ackerman, T. P., K. N. Liou, F. P. Valero, and L. Pfister (1988), Heating rates in tropical anvils, *J. Atmos. Sci.*, *45*, 1606–1623.
Baran, A. J., P. Hill, K. Furtado, P. Field, and J. Manners (2014), A coupled cloud physics–radiation parameterization of the bulk optical properties of cirrus and its impact on the Met Office Unified Model Global Atmosphere 5.0 configuration, *J. Climate*, *27*, 7725–7752.
Berry, E., and G. G. Mace (2013), Cirrus cloud properties and the large-scale meteorological environment: Relationships derived from A-Train and NCEP–NCAR reanalysis data, *J. Appl. Meteorol. Climatol.*, *52*, 1253–1276.
Bogdan, A., and M. J. Molina (2009), Why does large relative humidity with respect to ice persist in cirrus ice clouds?, *J. Phys. Chem. A*, *113*, 14,123–14,130.
Borg, L. A., R. E. Holz, and D. D. Turner (2011), Investigating cloud radar sensitivity to optically thin cirrus using collocated Raman lidar observations, *Geophys. Res. Lett.*, 38, L05807, doi:10.1029/2010GL046365.

Cady-Pereira, K. E., M. W. Shephard, D. D. Turner, E. J. Mlawer, S. A. Clough, and T. J. Wagner (2008), Improved daytime column-integrated precipitable water vapor from Vaisala radiosonde humidity sensors, *J. Atmos. Oceanic Tech.*, *25*, 873–883.

Clothiaux, E. E., K. P. Moran, B. E. Martner, T. P. Ackerman, G. G. Mace, T. Uttal, J. H. Mather, K. B. Widener, M. A. Miller, and D. J. Rodriguez (1999), The Atmospheric Radiation Measurement program cloud radars: Operational modes, *J. Atmos. Oceanic Tech.*, *16*, 819–827.

Comstock, J. M., T. P. Ackerman, and D. D. Turner (2004), Evidence of high ice supersaturation in cirrus clouds using ARM Raman lidar measurements, *Geophys. Res. Lett.*, *31*, L11106, doi:10.1029/2004GL019705.

Cziczo, D. J., K. D. Froyd, C. Hoose, E. J. Jensen, M. Diao, M. A. Zondlo, J. B. Smith, C. H. Twohy, and D. M. Murphy (2013), Clarifying the dominant sources and mechanisms of cirrus cloud formation, *Science*, *340*, 1320–1324.

Dzambo, A. M., D. D. Turner, and E. J. Mlawer (2016), Evaluation of two Vaisala RS92 radiosonde solar radiative dry bias correction algorithms, *Atmos. Meas. Tech.*, *9*, 1613–1626, doi:10.5194/amt-9-1613-2016.

Evans, S. M., and R. T. Marchand (2013), Description of SGP atmospheric states. [Available online at http://www.atmos.washington.edu/~roj/nobackup/Classification_Results/SGP/Description_of_SGP_states_2012.pdf.]

Evans, S. M., R. T. Marchand, T. P. Ackerman, and N. Beagley (2012), Identification and analysis of atmospheric states and associated cloud properties for Darwin, Australia, *J. Geophys. Res.*, *117*, D06204, doi:10.1029/2011JB008398.

Furtado, K., P. R. Field, R. Cotton, and A. J. Baran (2014), The sensitivity of simulated high clouds to ice crystal fall speed, shape and size distribution, *Q. J. Roy. Meteorol. Soc.*, *141*, 1546–1559, doi:10.1002/qj.2457.

Goff, J. A., and S. Gratch (1946), Low-pressure properties of water from −160 to 212 F, *Trans. Amer. Soc. Heat. Vent. Eng*, *51*, 125–164.

Haag, W., B. Kärcher, J. Ström, A. Minikin, U. Lohmann, J. Ovarlez, and A. Stohl (2003), Freezing thresholds and cirrus cloud formation mechanisms inferred from in situ measurements of relative humidity, *Atmos. Chem. Phys.*, *3*, 1791–1806.

Heymsfield, A. J., and L. M. Miloshevich (1995), Relative humidity and temperature influences on cirrus formation and evolution: Observations from wave clouds and FIRE II, *J. Atmos. Sci.*, *52*, 4302–4326.

Immler, F. J., J. Dykema, T. Gardiner, D. N. Whiteman, P. W. Thorne, and H. Vömel (2010), Reference Quality Upper-Air Measurements: Guidance for developing GRUAN data products, *Atmos. Meas. Tech.*, *3*, 1217–1231.

Kalesse, H., and P. Kollias (2013), Climatology of high cloud dynamics using profiling ARM Doppler radar observations, *J. Climate*, *26*, 6340–6359.

Kärcher, B., A. Dörnbrack, and I. Sölch (2014), Supersaturation variability and cirrus ice crystal size distributions, *J. Atmos. Sci.*, *71*, 2905–2926.

Kennedy, A., X. Dong, and B. Xi (2015), Cloud fraction at the ARM SGP site: Reducing uncertainty with self organizing maps, *Theor. Appl. Climatol.*, *124*, 43, doi:10.1007/s00704-015-1384-3.

Kollias, P., B. A. Albrecht, E. E. Clothiaux, M. A. Miller, K. L. Johnson, and K. P. Moran (2005), The Atmospheric Radiation Measurement program cloud profiling radars: An evaluation of signal processing and sampling strategies, *J. Atmos. Oceanic Tech.*, *22*, 930–948.

Kollias, P., M. A. Miller, E. P. Luke, K. L. Johnson, E. E. Clothiaux, K. P. Moran, K. B. Widener, and B. A. Albrecht (2007), The Atmospheric Radiation Measurement Program cloud profiling radars: Second-generation sampling strategies, processing, and cloud data products, *J. Atmos. Oceanic Tech.*, *24*, 1199–1214.

Liou, K. N. (1986), Influence of cirrus clouds on weather and climate processes: A global perspective, *Mon. Weather Rev.*, *114*, 1167–1199.

Mace, G. G., D. O.'. C. Starr, T. P. Ackerman, and P. Minnis (1995), Examination of coupling between an upper tropospheric cloud system and synoptic scale dynamics diagnosed from wind profiler and radiosonde data, *J. Atmos. Sci.*, *52*, 4094–4127.

Mace, G. G., E. E. Clothiaux, and T. P. Ackerman (2001), The composite characteristics of cirrus clouds: Bulk properties revealed by one year of continuous cloud radar data, *J. Climate*, *14*, 2185–2203.

Mace, G. G., S. Benson, and E. Vernon (2006), Cirrus clouds and the large-scale atmospheric state: Relationships revealed by six years of ground-based data, *J. Climate*, *19*, 3257–3278.

Marchand, R., N. Beagley, and T. P. Ackerman (2009), Evaluation of hydrometeor occurrence profiles in the multiscale modeling framework climate model using atmospheric classification, *J. Climate*, *22*, 4557–4573.

Miloshevich, L. M., H. Vömel, D. N. Whiteman, and T. Leblanc (2009), Accuracy assessment and correction of Vaisala RS92 radiosonde water vapor measurements, *J. Geophys. Res.*, *114*, D11305, doi:10.1029/2008JD011565.

Mitchell, D. L., S. Mishra, and R. P. Lawson (2011), Representing the ice fall speed in climate models: Results from Tropical Composition, Cloud and Climate Coupling (TC4) and the Indirect and Semi-Direct Aerosol Campaign (ISDAC), *J. Geophys. Res.*, *116*, D00T03, doi:10.1029/2010JD015433.

Moran, K. P., B. E. Martner, M. J. Post, R. A. Kropfli, D. C. Welsh, and K. B. Widener (1998), An unattended cloud-profiling radar for use in climate research, *Bull. Am. Meteorol. Soc.*, *79*, 443–455.

Muhlbauer, A., T. P. Ackerman, J. M. Comstock, G. S. Diskin, S. M. Evans, R. P. Lawson, and R. T. Marchand (2014), Impact of large-scale dynamics on the microphysical properties of midlatitude cirrus, *J. Geophys. Res. Atmos.*, *119*, 3976–3996, doi:10.1002/2013JD020035.

Ovarlez, J., P. Velthoven, G. Sachse, S. Vay, H. Schlager, and H. Ovarlez (2000), Comparison of water vapor measurements from POLINAT 2 with ECMWF analyses in high-humidity conditions, *J. Geophys. Res.*, *105*, 3737-3744, doi:10.1029/1999JD900954.

Pfister, L., et al. (2001), Aircraft observations of thin cirrus clouds near the tropical tropopause, *J. Geophys. Res.*, *106*, 9765–9786, doi:10.1029/2000JD900648.

Potter, B. E., and J. R. Holton (1995), The role of monsoon convection in the dehydration of the lower tropical stratosphere, *J. Atmos. Sci.*, *52*, 1034–1050.

Protat, A., S. A. Young, S. A. McFarlane, T. L'Ecuyer, G. G. Mace, J. M. Comstock, C. N. Long, E. Berry, and J. Delanoë (2014), Reconciling ground-based and space-based estimates of the frequency of occurrence and radiative effect of clouds around Darwin, Australia, *J. Appl. Meteor. Climatol.*, *53*, 456–478, doi:10.1175/JAMC-D-13-072.1.

Rowe, P. M., L. M. Miloshevich, D. D. Turner, and V. P. Walden (2008), Dry bias in Vaisala RS90 radiosonde humidity profiles over Antarctica, *J. Atmos. Oceanic Tech.*, *25*, 1529–1541.

Sassen, K., and J. R. Campbell (2001), A midlatitude cirrus cloud climatology from the Facility for Atmospheric Remote Sensing. Part I: Macrophysical and synoptic properties, *J. Atmos. Sci.*, *58*, 481–496.

Sassen, K., and V. I. Khvorostyanov (1998), Radar probing of cirrus and contrails: Insights from 2D model simulations, *Geophys. Res. Lett.*, *25*, 975–978, doi:10.1029/98GL00731.

Sisterson, D. L., R. A. Peppler, T. S. Cress, P. J. Lamb, and D. D. Turner (2016), The ARM Southern Great Plains (SGP) site, *The Atmospheric Radiation Measurement (ARM) program: The first 20 years. Meteor. Monograph, 57, Amer. Meteor. Soc.*, 13.1–13.18, doi:10.1175/AMSMONOGRAPHS-D-16-0004.1.

Spichtinger, P., K. Gierens, and H. Wernli (2005), A case study on the formation and evolution of ice supersaturation in the vicinity of a warm conveyor belt's outflow region, *Atmos. Chem. Phys.*, *5*, 973–987.

Stephens, G. L., et al, (2002), The CloudSat mission and the A-Train: A new dimension of space-based observations of clouds and precipitation, *Bull. Am. Meteorol. Soc.*, *83*, 1771–1790.

Turner, D. D., S. A. Clough, J. C. Liljegren, E. E. Clothiaux, K. E. Cady-Pereira, and K. L. Gaustad (2007), Retrieving liquid water wath and precipitable water vapor from the Atmospheric Radiation Measurement (ARM) microwave radiometers, *IEEE Trans. Geosci. Remote Sens.*, *45*(11), 3680–3690, doi:10.1109/TGRS.2007.903703.

Vömel, H., H. Selkirk, L. Miloshevich, J. Valverde-Canossa, J. Valdés, E. Kyrö, R. Kivi, W. Stolz, G. Peng, and J. A. Diaz (2007), Radiation dry bias of the Vaisala RS92 humidity sensor, *J. Atmos. Oceanic Tech.*, *24*, 953–963.

Währn, J., V. Oyj, I. Rekikoski, H. Jauhiainen, and J. Hirvensalo (2004), New Vaisala radiosonde RS92: Testing and results from the field In Eighth Symposium on Integrated Observing and Assimilation Systems for Atmosphere, Oceans, and Land Surface, American Meteorological Society.

Wang, J., L. Zhang, A. Dai, F. Immler, M. Sommer, and H. Vömel (2013), Radiation dry bias correction of Vaisala RS92 humidity data and its impacts on historical radiosonde data, *J. Atmos. Oceanic Tech.*, *30*, 197–214.

Wylie, D. P., W. P. Menzel, H. M. Woolf, and K. I. Strabala (1994), Four years of global cirrus cloud statistics using HIRS, *J. Climate*, *7*, 1972–1986.

Yang, P., B.-C. Gao, B. A. Baum, W. J. Wiscombe, Y. X. Hu, S. L. Nasiri, P. F. Soulen, A. J. Heymsfield, G. M. McFarquhar, and L. M. Miloshevich (2001), Sensitivity of cirrus bidirectional reflectance to vertical inhomogeneity of ice crystal habits and size distributions for two Moderate-Resolution Imaging Spectroradiometer (MODIS) bands, *J. Geophys. Res.*, *106*, 17,267–17,291, doi:10.1029/2000JD900618.

Yoneyama, K., M. Fujita, N. Sato, M. Fujiwara, Y. Inai, and F. Hasebe (2008), Correction for radiation dry bias found in RS92 radiosonde data during the MISMO field experiment, *SOLA*, *4*, 13–16.

Yu, H., P. E. Ciesielski, J. H. Wang, C. Kuo, H. Vömel, and R. Dirksen (2015), Evaluation of humidity correction methods for Vaisala RS92 tropical sounding data, *J. Atmos. Oceanic Tech.*, *32*, 397–411.